Design and Analysis of a 6-DoF Compliant Vibration Isolator for Small Satellite Optical Payloads Considering Ball-Joint Effects

Thien Nguyen Luong
Vietnam National Space Center, Vietnam Academy of Science and Technology, Vietnam
nlthien@vnsc.org.vn

Duc To Anh
Vietnam National Space Center, Vietnam Academy of Science and Technology, Vietnam
taduc@vnsc.org.vn

Huy Le Xuan
Vietnam National Space Center, Vietnam Academy of Science and Technology, Vietnam
lxhuy@vnsc.org.vn

Tuan Pham Anh
Vietnam National Space Center, Vietnam Academy of Science and Technology, Vietnam
patuan@vnsc.org.vn

Quan Pham Hong
Graduate University of Science and Technology, Vietnam Academy of Science and Technology, Vietnam
phquan@vnsc.org.vn

Ngoc Pham Van Bach
Vietnam National Space Center, Vietnam Academy of Science and Technology, Vietnam
pvbngoc@vnsc.org.vn (corresponding author)

Received: 16 January 2026 | Revised: 6 February 2026, 19 February 2026, 26 February 2026, and 28 February 2026 | Accepted: 2 March 2026

 DOI: https://doi.org/10.48084/etasr.17593

ABSTRACT

The performance of optical payloads on satellites is dependent on the mechanical stability of the satellite structure. Although spatial, spectral, temporal, and radiometric resolutions are commonly used to characterize image quality, these indicators do not adequately capture image degradation caused by micro-vibrations originating from satellite subsystems, such as driven motors, reaction wheels, control moment gyroscopes, cryo-coolers, and solar panel drive mechanisms, or structural resonances. In high-resolution optical payloads, low-frequency vibrations can induce image blur, pointing errors, and long-term structural fatigue, thereby reducing mission effectiveness. This study presents the design and analysis of a six-Degrees of Freedom (6-DoF) passive vibration isolation mechanism intended for optical payload stabilization of satellite platforms. The proposed device is based on a parallel compliant architecture derived from the Stewart-Gough platform with a specially shaped leg and ball joint. The kinematic behavior of the platform was first examined through Jacobian formulation and singularity analysis to ensure stable operation within the intended workspace. Based on this analysis, a compliant mechanism employing S-shaped flexible legs combined with spherical ball joints was developed to provide effective vibration attenuation while preserving high stiffness in non-motion directions. Dynamic simulations were conducted under harmonic base excitations with frequencies ranging from 5 to 25 Hz, representative of typical micro-vibration sources in satellite systems. The results demonstrate that the proposed isolator provides effective vibration attenuation in the low- and mid-frequency bands, with isolation efficiencies

increasing from approximately 5% at 5 Hz to about 56% at 20 Hz. At the upper limit of the investigated frequency range (25 Hz), a marked reduction in isolation efficiency was observed, indicating a degradation of isolation performance near this frequency. Nevertheless, the isolator maintained positive isolation behavior throughout the investigated range without exhibiting amplification effects. Comparative studies with alternative leg geometries further demonstrated the superiority of the proposed configuration in terms of isolation efficiency and dynamic stability. These results indicate that the proposed 6-DOF passive compliant mechanism is well-designed for enhancing the image quality and structural integrity of optical payloads in high-resolution remote sensing satellites.

Keywords-compliance; vibration isolator; small satellites; dynamic simulation; Stewart-Gough platform

I. INTRODUCTION

In the orbital flight of satellites, internal and external disturbances constitute a concern for high-precision optical payloads. Micro-vibrations generated by reaction wheels, flywheels, active thermal-control systems, and other onboard mechanisms [1-3], together with residual oscillations arising from deployable structures, such as antennas and solar arrays, can propagate through the flexible spacecraft structure. These effects are further compounded by low-frequency external torques induced by aerodynamic drag [4], gravity-gradient disturbances, and solar radiation pressure [5]. In particular, for small satellite platforms, where compact architectures and closely integrated subsystems facilitate disturbance transmission, such micro-vibrations can induce line-of-sight jitter, dynamic misalignment of optical components, degradation of the modulation transfer function, and ultimately a loss of image quality and pointing accuracy. Consequently, modern high-resolution imaging systems must explicitly account for these disturbances in their pointing-error budgets and adopt appropriate mitigation strategies at both the structural and system levels.

To address vibration-induced performance degradation, a range of isolation approaches have been investigated. Passive solutions, including elastomeric or viscoelastic mounts and tuned mass dampers, are widely employed due to their simplicity, reliability, and low power requirements. However, their effectiveness is typically limited to low frequencies and is often confined to one or two motion directions [6, 7]. Active vibration control systems based on piezoelectric or voice-coil actuators can achieve superior attenuation, yet their reliance on sensors, control algorithms, and continuous power supply restricts their applicability in small satellite missions with stringent resource constraints [8]. More recently, multi-Degrees of Freedom (DoF) passive isolators based on parallel mechanisms, particularly Stewart-platform architectures, have attracted attention owing to their ability to simultaneously attenuate coupled translational and rotational disturbances while maintaining high stiffness, compactness, and precise optical alignment [9]. Despite these advances, there is a need for compact, fully passive isolation solutions capable of providing effective low-frequency attenuation in all six-Degrees of Freedom (6-DoF) while satisfying the strict mass, volume, and reliability requirements of small satellite optical payloads.

Studies on spacecraft micro-vibrations have shown that the dynamic disturbances affecting optical payloads on small satellite platforms can be classified into low-, medium-, and high-frequency components according to their physical origins and transmission characteristics [6]. Low-frequency disturbances, typically below 10 Hz, are mainly associated with flexible structural modes, thermal deformations, and orbital environmental effects, whereas medium-frequency micro-vibrations, generally ranging from several Hz to a few tens of Hz, are predominantly generated by onboard mechanical devices, such as reaction wheels and cryocoolers, commonly used in small satellites. These medium-frequency micro-vibrations have the most significant impact on optical payload performance, as they directly induce line-of-sight jitter and degradation of modulation transfer function in high-resolution imaging systems. In contrast, high-frequency disturbances in the hundreds of Hz to kHz range are largely attenuated through structural transmission and have a limited influence on the payload pointing stability. Accordingly, the frequency range of 5–25 Hz was identified as the most critical band for assessing the micro-vibration isolation performance in small satellite optical payloads and was therefore selected for a detailed dynamic analysis in this study. The dynamic vibration response of optical payloads under harmonic excitation is governed by resonance-induced amplification and vibration transmissibility. As shown in [10], when the excitation frequencies approach the natural frequencies of a mechanical system, parallel or lumped configurations may exhibit significant dynamic amplification owing to stiffness degradation and force–motion coupling effects. In Stewart-platform-based structures, such behavior is configuration-dependent and can be directly characterized by the Jacobian matrix, where ill-conditioned or near-singular configurations lead to reduced effective stiffness and increased vibration response. Therefore, Jacobian and singularity analyses are essential to ensure stable dynamic behavior and effective vibration isolation in parallel compliant mechanisms.

This study proposes a novel passive 6-DoF compliant vibration isolator employing a Stewart-platform-inspired architecture with S-shaped flexible legs and spherical ball joints, which is specifically tailored for small satellite optical payloads. The proposed design aims to enhance low-frequency vibration isolation while preserving structural stability and alignment accuracy, thereby improving the operational performance of spaceborne imaging systems. This research focused on a parallel structure and proposed passive vibration isolator devices that can isolate small vibrations. The parallel structure is a closed-loop mechanism in which the movable side is connected to the base by at least two independent kinematic chains. With multiple closed loops, the stiffness of the entire mechanism can be improved because all the pin connectors maintain the load in a distributed manner. The problem of end-point positioning error is also reduced because there is no accumulation of errors. The parallel structure has

the advantages of compactness, high speed, high precision, high load capacity and high rigidity compared with the series structure. However, the disadvantage is that the working space is limited due to the limitations of the connector activation and interference.

This study first investigated the Jacobian and singular conditions of the Stewart-Gough platform [11]. Then, a 6-DoF compliance mechanism was designed using a parallel structure and the dynamics were simulated to evaluate the working efficiency when changing some parts of the structure.

II. JACOBIAN AND SINGULARITY ANALYSIS

Initially, this work investigates the Jacobian and singular condition of the Stewart–Gough platform, as shown in Figure 1.

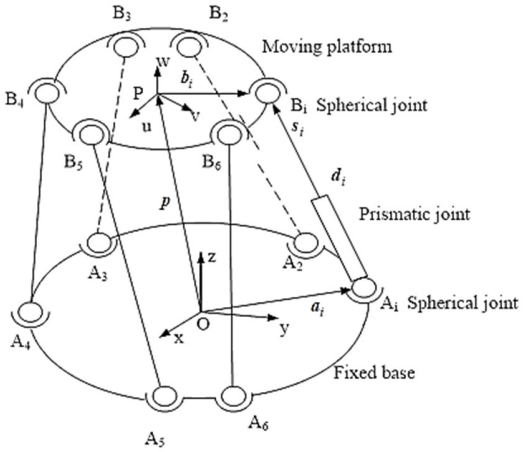

Fig. 1. Kinematic configuration of a Gough-Stewart platform.

The given input vector is $\dot{\boldsymbol{q}} = [\dot{l}_1, \dot{l}_2, \ldots, \dot{l}_6]^T$ and the output vector can be described by the velocity of the center point and the angular velocity of the moving platform:

$$\dot{\boldsymbol{p}} = \begin{bmatrix} \boldsymbol{v}_P \\ \boldsymbol{\omega}_B \end{bmatrix} \tag{1}$$

The Jacobian matrix can be derived from the formulation of a closed-loop velocity equation for each limb. The closed-loop equation for each limb can be written as:

$$\overline{OP} + \overline{PB_i} = \overline{OA_i} + \overline{A_iB_i} \tag{2}$$

The position vector $\boldsymbol{p}$ and rotation matrix ${}^A R_B$ of frame $\{B\}$ with respect to $\{A\}$, given the limb length l_i for $i = 1,2\ldots,6$, are to be found. The solution is straightforward:

$$l_i^2 = [\boldsymbol{p} + {}^A R_B \, {}^B\boldsymbol{b}_i - \boldsymbol{a}_i]^T [\boldsymbol{p} + {}^A R_B \, {}^B\boldsymbol{b}_i - \boldsymbol{a}_i]$$

$$l_i^2 = \boldsymbol{p}^T\boldsymbol{p} + [{}^B\boldsymbol{b}_i]^T[{}^B\boldsymbol{b}_i] + \boldsymbol{a}_i^T\boldsymbol{a}_i + 2\boldsymbol{p}^T[{}^A R_B \, {}^B\boldsymbol{b}_i] - 2\boldsymbol{p}^T\boldsymbol{a}_i - 2[{}^A R_B \, {}^B\boldsymbol{b}_i]^T\boldsymbol{a}_i \text{ for } i = 1,2\ldots,6 \tag{3}$$

for $i = 1,2\ldots,6$.

Differentiating (3) with respect to time yields:

$$\boldsymbol{v}_p + \boldsymbol{\omega}_B \times \boldsymbol{b}_i = l_i\boldsymbol{\omega}_i \times \boldsymbol{s}_i + \dot{l}_i\boldsymbol{s}_i \tag{4}$$

where $\boldsymbol{b}_i$ and $\boldsymbol{s}_i$ denote the vector $\overline{PB_i}$ and unit vector along $\overline{A_iB_i}$, respectively, and $\boldsymbol{\omega}_i$ denotes the angular velocity of the i^{th} limb with respect to the fixed frame $Oxyz$.

To eliminate $\boldsymbol{\omega}_i$, we dot-multiply both sides of (2) by $\boldsymbol{s}_i$:

$$\boldsymbol{s}_i \cdot \boldsymbol{v}_p + (b_i \times \boldsymbol{s}_i) \cdot \boldsymbol{\omega}_B = \dot{l}_i \tag{5}$$

Equation (2) written six times, once for each $i = 1,2\ldots,6$, yields six scalar equations, which can be assembled in matrix form:

$$\boldsymbol{J}_x\dot{\boldsymbol{p}} = \boldsymbol{J}_q\dot{\boldsymbol{q}} \tag{6}$$

$$\text{where } \boldsymbol{J}_x = \begin{bmatrix} \boldsymbol{s}_1^T & (\boldsymbol{b}_1 \times \boldsymbol{s}_1)^T \\ \boldsymbol{s}_2^T & (\boldsymbol{b}_2 \times \boldsymbol{s}_2)^T \\ \vdots & \vdots \\ \boldsymbol{s}_6^T & (\boldsymbol{b}_6 \times \boldsymbol{s}_6)^T \end{bmatrix} \text{ and } \boldsymbol{J}_q = \boldsymbol{I}_{6\times6} \tag{7}$$

Equation (6) can be rewritten as:

$$\dot{\boldsymbol{q}} = \boldsymbol{J}\dot{\boldsymbol{p}} \tag{8}$$

where the Jacobian matrix can be expressed as:

$$\boldsymbol{J} = {\boldsymbol{J}_q}^{-1}\,\boldsymbol{J}_x \tag{9}$$

where $\boldsymbol{J}$ is the Jacobian matrix of Stewart-Gough platforms.

Let $\boldsymbol{n}_i = \boldsymbol{b}_i \times \boldsymbol{s}_i$ (10)

Then $\boldsymbol{n}_i$ represents a vector that is normal to the plane containing points A_i, B_i, and P. In the following, we discuss the physical meaning of the three types of singularities. Inverse kinematic singularities cannot occur with the workspace of the manipulator since $\boldsymbol{J}_q$ is identity matrix.

However, inverse kinematic singularities can occur at the workspace boundary, where one or more limbs are in fully stretched or retracted positions. Direct kinematic singularities are difficult to solve. Although it is impossible to find all singularities, some of them can be identified by an examination of the matrix $\boldsymbol{J}_x$. For example, when the moving platform falls on top of the fixed base, $\boldsymbol{n}_i = 0$, identically, for $i = 1,2\ldots,6$. The manipulator gains to 3 DoF. That is, the moving platform can perform an infinitesimal rotation about any axis on the *x*-*y* plane. Moreover, an infinitesimal translation along the *z*-axis can be performed. Another direct kinematic singularity occurs when the geometry of the manipulator satisfies the following conditions: the geometry of the moving platform is identical to that of the fixed platform, the manipulator assumes a configuration in which the limb lengths are equal to one another, and all the limbs are parallel to each other. When the foregoing conditions are met, the moving platform gains two translational degrees of freedom. Namely, it can be positioned anywhere on a spherical surface of a radius equal to the length of a limb and centered at the geometric center of the fixed platform. The orientation of the moving platform remains unchanged throughout this motion. There are infinitely many such configurations, whenever the condition $l_1 = l_2 = \cdots = l_6$ is met. Finally, a combined singularity cannot occur within the workspace of the manipulator since $\boldsymbol{J}_q$ is an identity matrix.

III. DESIGN OF 6-DOF COMPLIANCE MECHANISM AND BALL-JOINT

The design of the compliance mechanism includes the design of the parts: the bases (mobile and fixed), joints, and legs. Different compliance mechanism designs primarily focus on the design of the legs and joints.

A. Design of Joints

Many types of flexure joints have been researched and developed, most of which fall into two categories: notch joints and springs. Notch type flexure joints were first analyzed in [12] and have since been developed by many researchers and designers. Today, notch-type joint assemblies are widely used for small displacement, high precision mechanisms [13]. These joints were also applied in [14] to develop the field of pseudo-rigid-body compliant mechanisms. Spring joints provide a linear joint consisting of parallel beam sets. In addition to high-precision motions, spring joints are widely employed in medical instrumentation [15] and microelectromechanical devices [16]. The benefits obtained from the use of flexure joints are often accompanied by certain disadvantages that must be considered in the design. To overcome these disadvantages and develop better flexural capabilities, a set of criteria must be established. The four most important criteria are the range of motion or working space, the axial sliding capacity, the ratio of off axis to axial stiffness, and the influence of stress concentration. Many revolute joints have also been created using a combination of notch-type and leaf springs.

Some common types of joints used today include ball, Hooke, and sliding joints. Ball joints are spherical bearings that connect the control arms to the steering knuckles and are used in most manufactured cars. Technically, they are similar to the ball and socket joints found in most quadrupeds. The ball joints consist of a bearing pin and socket housed in a housing, all of which are made of steel. The bearing stud is tapered and threaded, and fits into a tapered hole in the steering knuckle. The housing prevents dirt from entering the joint assembly. Typically, this is a rubber-like boot that allows lubricant to move and expand. Ball joints that control motion tend to be retained by an internal spring, which helps to prevent vibration problems in the linkage. Ball joints are utilized to allow free rotation in two planes at the same time while preventing displacement in any direction. A Hooke's joint, also known as a universal joint or a U-joint, is a joint or coupling that joins rigid shafts which are inclined to each other. It is commonly used in shafts that transmit rotary motion. It consists of a pair of hinges located close together, oriented at an angle of 90° to each other, and connected by a cross shaft. A sliding joint is a mechanical structure that enables linear extension and compression. Sliding joints can be designed to allow the continuous relative motion of two parts, or they can be adjusted by removing the clamp from a fixed position and clamping it again in a different position. They use a hinge to hold the parts apart, but can slide together for transport.

After analyzing the advantages and disadvantages of each type of joint, a ball joint was chosen for the proposed design. The detailed design of the joint is presented in Figure 2.

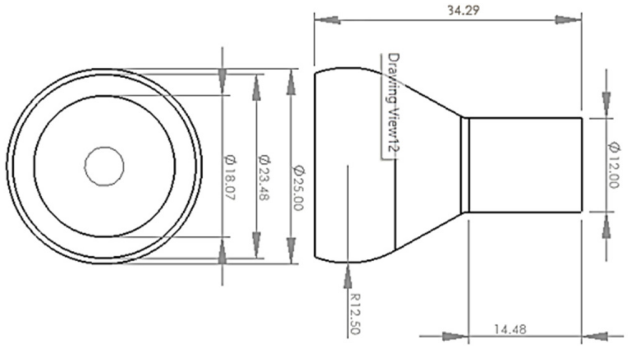

Fig. 2. Ball joint detailed design.

B. Design of Legs and Complete Compliance Mechanism

This study used the S-shaped leg structure, as illustrated in Figure 3. The parameters of the mechanism are listed in Table I, as presented in [17]. The difference between these two studies is in the design of the joint. In [17], an absolutely rigid connection was used rather than a joint connection to evaluate the simulation between the leg and platform. For low-frequency vibrations, the clearance between the ball of joint and the cover of joint is very important, impacting precision components like optics or antennas in small satellites. This gap controls wear, friction, and potential rattling (micro-vibrations), often requiring specialized designs (like magnetic bearings) or damping to prevent damage and maintain mission performance in sensitive instruments.

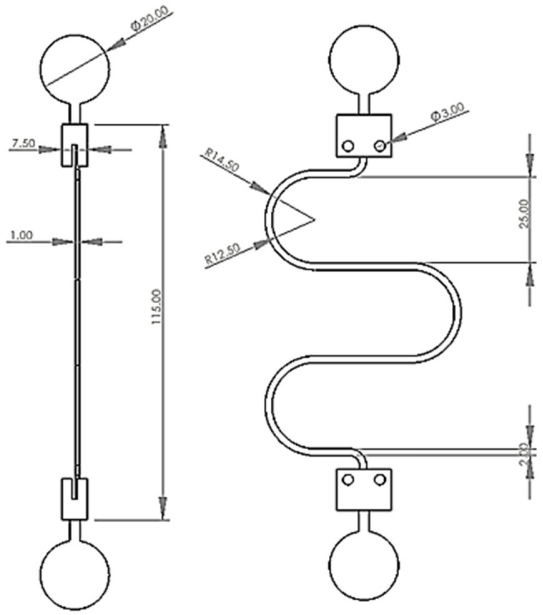

Fig. 3. Detailed design of the legs.

For the proposed geometric parameters, the nominal operating configuration of the compliant mechanism remained well within the regular workspace. The Jacobian matrix was well conditioned throughout the expected small-displacement range, with no indication of proximity to forward or inverse kinematic singularities. Given that vibration-induced motions are extremely small compared to the geometric dimensions of

the mechanism, the risk of approaching singular configurations during operation is negligible.

TABLE I. PARAMETERS OF COMPLIANCE

Dimension of moving base r_b	106 mm
Dimension of fixed base r_a	134 mm
Length of leg (initial) L_0	180 mm
Height (initial) h_0	214 mm
Thickness of leg	2 mm
Radius of curvature (of leg)	17.5 mm
Half angles of the adjacent spherical joints j_a	6.9^0
Half angles of the adjacent spherical joints j_b	11.3^0

IV. SIMULATION ANALYSIS OF 6-DOF COMPLIANCE MECHANISM CONSIDERING THE EFFECT OF BALL JOINTS

To ensure the reproducibility of the numerical results, all geometrical parameters, boundary conditions, excitation characteristics, joint models, and evaluation metrics used in the dynamic simulations are summarized in Table II.

TABLE II. SIMULATION SETTINGS AND PARAMETERS

Simulation type	Time-domain dynamic
Excitation form	Harmonic force
Force amplitude	30 N
Frequency range	5, 10, 15, 20, 25 Hz
Payload mass	1.5 kg
Joint model	Spherical (joint) / Rigid (without joint)
Boundary condition	Fixed base fully constrained
Output metric	Acceleration transmissibility
Material properties	Same as in [17]
Response evaluation	Steady-state peak acceleration amplitude

All simulation cases were performed under identical settings, with only the joint configuration varying for comparison. The simulations were carried out using the Ansys Mechanical software. The harmonic response analysis was performed utilizing a frequency-domain solver with the full method. For time-domain verification, a fixed time step of $\Delta t = 1\times10^{-4}$ s and a total duration of 5 s were used. Steady-state was assumed when the peak displacement amplitude variation between two consecutive cycles was less than 1%. The ball joints were modeled as ideal spherical joints without friction or backlash. In the proposed model, ball joints were represented as ideal spherical joints, providing rotational freedom without clearance, friction, or contact nonlinearity. This assumption allows the first-order influence of joint-induced constraint modification on the dynamic behavior to be isolated. Modeling of frictional effects and clearance-induced nonlinearities will be considered in future studies. The applied harmonic force was utilized as a normalized excitation input for comparative evaluation of isolation performance. Owing to the linear elastic assumption, the obtained isolation efficiencies are independent of the excitation amplitude and remain applicable to realistic micro-vibration levels. The frequency-domain assessment was conducted using discrete harmonic response analyses at excitation frequencies of 5, 10, 15, 20, and 25 Hz. Each frequency point was solved independently under steady-state conditions and no continuous frequency sweep was performed.

Figures 4-8 show the acceleration results of the upper plate over time. From the time-domain acceleration plots, the vibration responses of the upper and lower plates exhibit similar temporal trends, and no significant phase difference is visually distinguishable at the scale of the presented figures/ Figures 4-8. The calculated isolation capacity at different frequencies was 5.39% (5 Hz), 22.86% (10 Hz), 50.29% (15 Hz), 56.35% (20 Hz), and 2.63% (25 Hz). In the dynamic simulations, the ball joints were modeled as spherical joints with rotational degrees of freedom and high translational stiffness, thereby explicitly accounting for their rotational compliance in the system Jacobian and dynamic response. As shown in Figure 9, the 6-DoF compliant device using the S-shaped leg configuration and ball joint isolates more effectively than the device without a ball joint (the isolation efficiency can reach 60%). In the frequency range of less than 25 Hz, this compliant device always isolates effectively (no negative isolation performance). This can be explained by the fact that the ball joint design and its use satisfied the four requirements presented above, especially the requirement of a high off-axis stiffness ratio compared to the stiffness in the direction of motion.

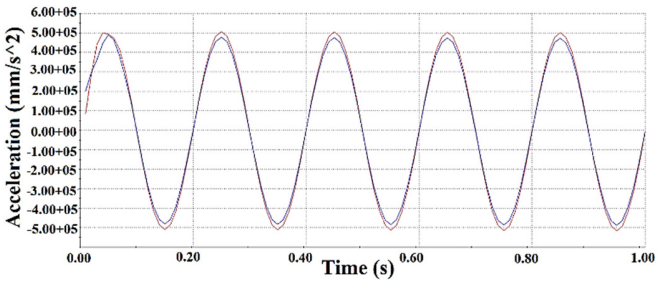

Fig. 4. Illustration of the acceleration of the fixed plate (red) and moving plate (blue) at 5 Hz.

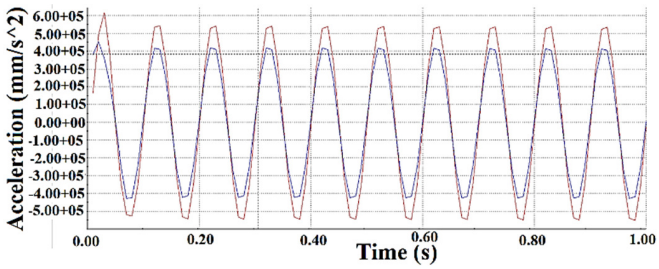

Fig. 5. Illustration of the acceleration of the fixed plate (red) and moving plate (blue) at 10 Hz.

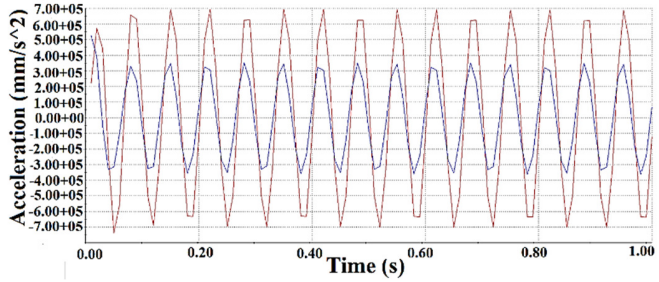

Fig. 6. Illustration of the acceleration of the fixed plate (red) and moving plate (blue) at 15 Hz.

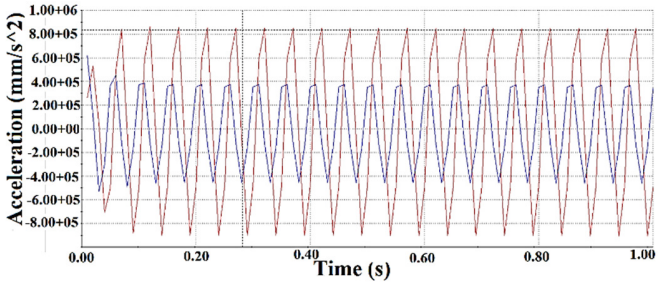

Fig. 7. Illustration of the acceleration of the fixed plate (red) and moving plate (blue) at 20 Hz.

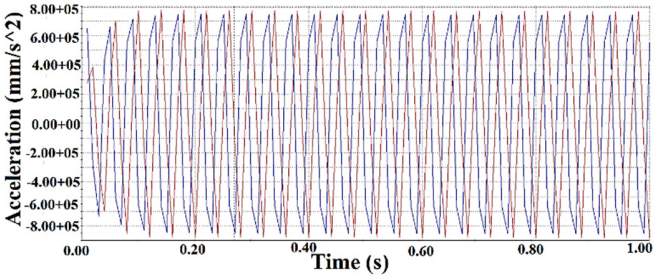

Fig. 8. Illustration of the acceleration of the fixed plate (red) and moving plate (blue) at 25 Hz.

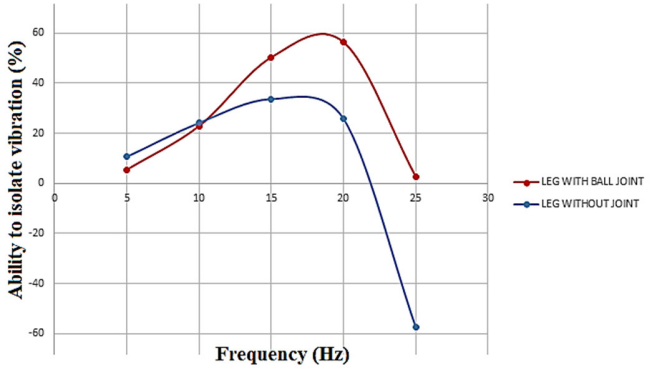

Fig. 9. Comparison of isolation vibration at different frequencies with and without ball joints

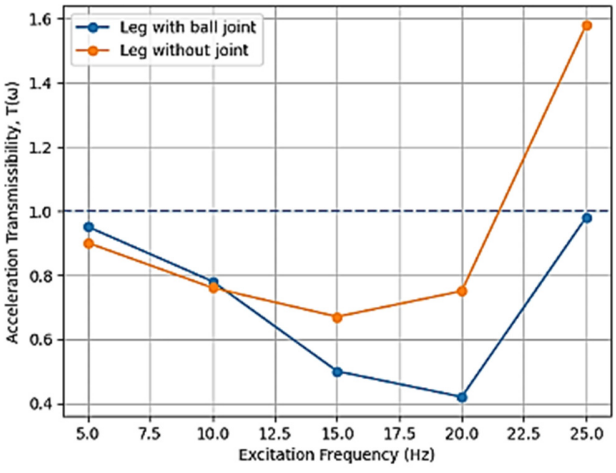

Fig. 10. Frequency-response-based acceleration transmissibility.

Frequency-response-based transmissibility and modal characteristics are shown in Figure 10. Acceleration transmissibility is defined as the ratio between the peak steady-state acceleration amplitude of the upper platform and that of the base excitation. The isolation efficiency is calculated as $\eta=(1-T\alpha)\times100\%$, based on the peak amplitudes obtained from the harmonic response analysis. The transmissibility $T\alpha$ is reconstructed from steady-state acceleration ratios at discrete excitation frequencies (5–25 Hz). Values below unity indicate vibration attenuation, whereas values above unity (observed for the rigid-joint configuration at 25 Hz) indicate resonance-induced amplification. The smoother attenuation trend obtained with the ball joints reflects improved low-frequency modal behavior. With the same leg length and ball joint size, three additional leg shapes are proposed, as shown in Figure 11.

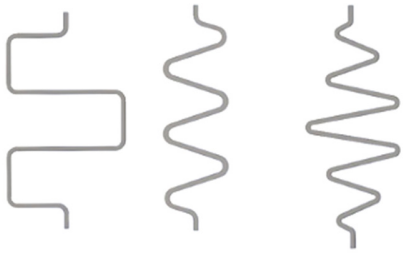

Fig. 11. Three proposed leg designs (Types I, II, and III).

This study also simulated the oscillations for the three proposed leg designs. The isolation efficiency results of the compliant device with different leg connection shapes are displayed in Figure 12.

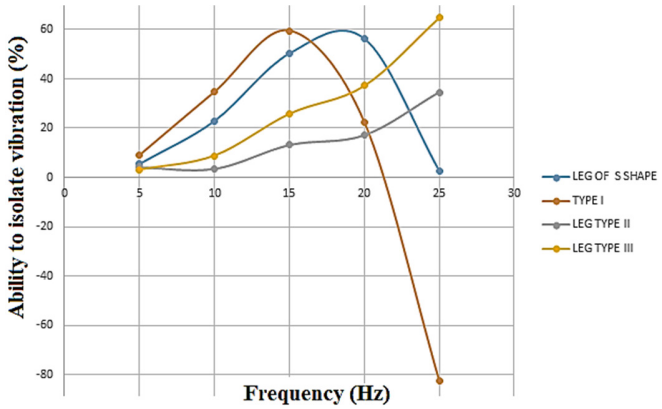

Fig. 12. Comparison of isolation vibration at different frequencies when using different leg shapes.

The pronounced drop in isolation efficiency observed for all leg configurations near 25 Hz and the vibration amplification exhibited by the Type I design suggest that the excitation frequency approaches the fundamental resonance of the compliant system. This resonance-related behavior is governed by the combined effects of mass–stiffness distribution, configuration-dependent dynamic stiffness, and force–motion coupling inherent to parallel compliant mechanisms. A detailed modal and frequency-response

analysis is therefore required to precisely identify the natural frequencies and damping characteristics of each configuration and will be addressed in future work. The present simulations assumed linear elastic behavior with implicit proportional damping. While sufficient for comparative assessment of isolation performance, explicit modeling of material and joint damping are essential for accurate prediction of resonance amplitudes.

V. CONCLUSIONS

In this study, the model parameters of a compliance device using an S-shaped leg with ball joint were determined from the results of calculations and simulations. The kinematic behavior of the proposed mechanism was first analyzed through Jacobian formulation and singularity analysis to ensure stable configurations and to avoid stiffness degradation associated with near-singular conditions. Based on this analysis, a compliant parallel mechanism was designed and evaluated through dynamic simulations under harmonic excitations representative of typical micro-vibration sources in small satellite systems. The introduction of spherical ball joints significantly alters the boundary conditions and dynamic behavior compared with rigidly connected compliant legs, highlighting the importance of joint modeling in parallel vibration isolators. The simulation results demonstrate that the proposed isolator provides effective vibration attenuation in the low- and mid-frequency ranges, with the isolation efficiency increasing progressively from low frequencies and reaching a maximum of approximately 56% at 20 Hz. At the upper limit of the investigated frequency range (25 Hz), a pronounced reduction in the isolation efficiency was observed, indicating a degradation of the isolation performance near this frequency. Nevertheless, the isolation efficiency remained positive across the entire investigated range, and no vibration amplification was detected. Comparative analyses with alternative leg geometries further confirmed that the S-shaped leg configuration combined with spherical ball joints offers superior isolation performance and improved dynamic stability over most of the targeted frequency band. These findings indicate that the proposed six-Degrees of Freedom (6-DoF) passive compliant mechanism is well-suited for mitigating dominant micro-vibrations affecting optical payloads in small satellites, particularly within the frequency range of 20 Hz.

Future work will focus on structural optimization, prototype fabrication, and experimental validation to further assess the performance and practical applicability in spaceborne environments. The present study was conducted under isothermal assumptions. Thermal deformation and thermomechanical coupling, which may influence the preload and isolation characteristics in space environments, were not considered and will be addressed in future work.

DECLARATION OF COMPETING INTERESTS

The authors declare that they have no known competing financial interests or personal relationships that could have appeared to influence the work reported in this paper.

ACKNOWLEDGMENT

The authors would like to acknowledge the financial support from the Vietnam Academy of Science and Technology (Grant number NVCC39.01/22-23).

DATA AVAILABILITY

The data supporting the findings of this study are available within the article. Additional data can be provided by the corresponding author upon reasonable request.

AI USE AND DECLARATION OF GENERATIVE AI USE

During the preparation of this work, the authors used ChatGPT only for limited language editing support to improve the clarity and readability of the manuscript. The scientific content, methodology, analysis, and conclusions were developed entirely by the authors. The AI tool was not used to generate, interpret, or validate any research results. All outputs were carefully reviewed, revised, and verified by the authors, who take full responsibility for the content of this publication.

REFERENCES

[1] R. A. Masterson, D. W. Miller, and R. L. Grogan, "Development and Validation of Reaction Wheel Disturbance Models: Empirical Model," *Journal of Sound and Vibration*, vol. 249, no. 3, pp. 575–598, Jan. 2002, https://doi.org/10.1006/jsvi.2001.3868.

[2] D.-K. Kim, "Micro-vibration model and parameter estimation method of a reaction wheel assembly," *Journal of Sound and Vibration*, vol. 333, no. 18, pp. 4214–4231, Sept. 2014, https://doi.org/10.1016/j.jsv.2014.04.032.

[3] S.-C. Kwon, S.-H. Jeon, and H.-U. Oh, "Performance evaluation of spaceborne cryocooler micro-vibration isolation system employing pseudoelastic SMA mesh washer," *Cryogenics*, vol. 67, pp. 19–27, Apr. 2015, https://doi.org/10.1016/j.cryogenics.2015.01.002.

[4] H.-Q. Li, X.-F. Liu, S.-J. Guo, and G.-P. Cai, "Deployment dynamics and control of large-scale flexible solar array system with deployable mast," *Advances in Space Research*, vol. 58, no. 7, pp. 1288–1302, Oct. 2016, https://doi.org/10.1016/j.asr.2016.06.008.

[5] T. Inamori, N. Sako, and S. Nakasuka, "Magnetic dipole moment estimation and compensation for an accurate attitude control in nano-satellite missions," *Acta Astronautica*, vol. 68, no. 11, pp. 2038–2046, June 2011, https://doi.org/10.1016/j.actaastro.2010.10.022.

[6] X. Jiao, J. Zhang, W. Li, Y. Wang, W. Ma, and Y. Zhao, "Advances in spacecraft micro-vibration suppression methods," *Progress in Aerospace Sciences*, vol. 138, Apr. 2023, Art. no. 100898, https://doi.org/10.1016/j.paerosci.2023.100898.

[7] Z. He *et al.*, "Progress of Stewart Vibration Platform in Aerospace Micro–Vibration Control," *Aerospace*, vol. 9, no. 6, June 2022, Art. no. 324, https://doi.org/10.3390/aerospace9060324.

[8] Q. Han, S. Gao, and F. Chu, "Micro-Vibration Analysis, Suppression, and Isolation of Spacecraft Flywheel Rotor Systems: A Review," *Vibration*, vol. 7, no. 1, pp. 229–263, Mar. 2024, https://doi.org/10.3390/vibration7010013.

[9] Y. P. Singh, N. Ahmad, and A. Ghosal, "Dynamically isotropic Gough–Stewart platform for micro-vibration isolation in spacecrafts," *Mechanism and Machine Theory*, vol. 201, Oct. 2024, Art. no. 105735, https://doi.org/10.1016/j.mechmachtheory.2024.105735.

[10] F. A. Jabbar, P. S. Rao, and S. O. W. Khafaji, "Enhancing the Design of Dynamic Vibration Absorbers through Harmonic Analysis and Lumped Parallel Configuration," *Engineering, Technology & Applied Science Research*, vol. 14, no. 5, pp. 16624–16639, Oct. 2024, https://doi.org/10.48084/etasr.7990.

[11] D. Stewart, "A Platform with Six Degrees of Freedom," *Proceedings of the Institution of Mechanical Engineers*, vol. 180, no. 1, pp. 371–386, June 1965, https://doi.org/10.1243/PIME_PROC_1965_180_029_02.

[12] J. M. Paros and L. Weisbord, "Flexure Hinges," *Machine Design*, vol. 37, pp. 151–156, 1965.

[13] E. Pernette, S. Henein, I. Magnani, and R. Clavel, "Design of parallelrobots in microrobotics," *Robotica*, vol. 15, no. 4, pp. 417–420, July 1997, https://doi.org/10.1017/S0263574797000519.

[14] L. L. Howell and A. Midha, "A Method for the Design of Compliant Mechanisms With Small-Length Flexural Pivots," *Journal of Mechanical Design*, vol. 116, no. 1, pp. 280–290, Mar. 1994, https://doi.org/10.1115/1.2919359.

[15] S. T. Smith, *Flexures: elements of elastic mechanisms*. Amsterdam: Gordon & Breach, 2000.

[16] L. Saggere, S. Kota, and S. B. Crary, "A New Design for Suspension of Linear Microactuators," in *ASME 1994 International Mechanical Engineering Congress and Exposition*, Nov. 1994, pp. 671–675, https://doi.org/10.1115/IMECE1994-0490.

[17] M. Hung Vu, N. Pham Van Bach, T. Nguyen Luong, and T. Bui Trung, "Kinematics design and statics analysis of novel 6-DOF passive vibration isolator with S-shaped legs based on Stewart platform," *Journal of Vibroengineering*, vol. 26, no. 1, pp. 66–78, Feb. 2024, https://doi.org/10.21595/jve.2023.23511.